

TES Bolometers

Miles Wu (advisor: Prof. Staggs)

January 4, 2011

Abstract

Transition edge sensor (TES) bolometers are increasingly being used as sensitive devices for measuring incoming photon radiation. These bolometers consist of an absorptive element connected to a heat bath. The temperature is measured by the change in resistance of a superconducting film, which is placed in the transition region. A simple one-block model for the the complex impedance of a TES bolometer is derived. This is compared against experimental data using a least squares algorithm and found to be less than ideal at the high frequency range. A couple of extensions to the model are proposed and tested against the data. One of these two-block models is found to be much more accurate compared to the one-block model, whilst the other provides only very modest improvements. A best estimate for the various TES parameters is then produced by averaging across many supposedly identical sensors. The results are then discussed in a physical context.

Contents

1	Introduction	3
2	The Basic Model	4
2.1	Linearization	4
2.2	The coupled differential equations	6
2.2.1	Electrical	6
2.2.2	Thermal	7
2.2.3	Matrix	7
3	Complex Impedance	7
3.1	Derivation	7
4	Data Analysis	8
4.1	Transfer Function	8
4.2	Initial look at the data	9
4.3	Fitting	9
4.4	Ideal TES	11
5	Extensions to the ideal TES model	11
5.1	Two block models	11
5.1.1	The derivation of the intermediate-block model	12
5.1.2	Fitting with multiple blocks	13
5.1.3	The results of the intermediate-block model fitting	14
5.1.4	The hanging-block model	14
5.2	Verification	15
5.3	Beyond two blocks	16

6	The Full Data Set	18
6.1	Going beyond one sensor	19
6.2	Higher temperature	19
7	Conclusion	22
8	References	22
9	Source Code	23

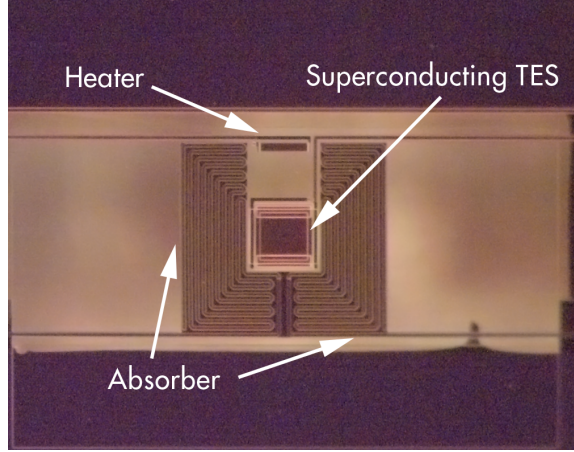


Figure 1: A labelled photograph illustrating the physical layout of a TES bolometer. The heater is used to bias the superconducting TES into the transition region, whilst the absorber converts the incoming photon power to heat and channels that into the TES. The whole system is mounted on a silicon nitride substrate and is connected to a heat bath via a weak thermal link. Photograph courtesy of S. Staggs.

1 Introduction

When certain materials are cooled to temperatures near absolute zero, they transition to a state where they have an electrical resistance of zero. This phenomenon is known as superconductivity and was explained by Bardeen, Cooper and Schreiffer in what has become known as BCS theory [2]. This theory states that pairs of free electrons in the lattice that normally carry the electricity can drop into a lower energy state known as a Cooper pair. These Cooper pairs then act like bosons and by forming a large Bose-Einstein condensate are able to transmit charge without any resistance. At high temperatures this does not happen as the thermal vibrations of the material prevents the electrons from going into this lower energy state. On the other hand, at very low temperatures the electrons can and superconductivity occurs.

However, around the superconducting transition temperature (known as the critical temperature), the material neither has a normal resistance nor a zero resistance, but something in between. This finite transition width is due to statistical thermal fluctuations in the material. This randomly gives some of the electrons enough energy to overcome the Cooper pair energy gap and become normal conductive electrons. The higher the temperature, the more Cooper pairs are broken, and the higher the resistance.

Transition edge sensor (TES) bolometers are made up of three main components. An annotated photograph illustrating the TES bolometer layout is shown in Figure 1. The maze-like path on the outside is the absorber, where the incident photons collide and cause it to heat up. This heat is then carried via a couple of small legs at the bottom into the central superconducting square, which is the TES itself. There is also a heater near the top which is used to bias the superconducting TES into its transition region. The whole device is connected to a heat bath via a weak thermal link. This ensures that the TES is kept around the transition temperature and takes the incoming power away, yet because it is only a weak link, it provides a response that can be measured.

Transition edge sensors exploit superconductivity's sharp transition to become highly sensitive thermometers. As the incident photons hit the absorber, they heat up the superconducting square, raising the resistance. This change in resistance can then be measured accurately via an electrical circuit. This bolometer setup allows for the energy of incident photons, such as microwaves, to be determined with great sensitivity.

Although modelling the TES bolometer is not strictly necessary in order to use one to measure incoming photon power, understanding its behaviour through modelling is important because it can inform the design

of future TES bolometers and provide insight on how to most optimally use them. This paper aims to derive a simple model of the TES bolometer and examine its validity.

2 The Basic Model

The TES bolometer has both thermal and electrical components, which are coupled together. For example, the TES is heated up by the Joule heating caused by electrical current and the non-zero resistance, yet the temperature affects the resistance. The derivation of this basic model closely follows the one given by Irwin and Hilton (2005) [4, p.7]. Let us first derive the basic equations that govern this system.

Thermally the TES is described in Figure 2. The TES, at temperature T and with a heat capacity of C , is connected to the heat bath via a thermal link with conductivity G . Heat flows arrives into the TES from the photon input, P , and the Joule heating (the I^2R term), P_{joule} , and escapes to the heat bath, P_{bath} . Just from adding up the heat flow we obtain:

$$C \frac{dT}{dt} = P_{joule} + P - P_{bath}. \quad (1)$$

Electrically the TES read-out circuit consists of a shunt resistor in parallel with the superconducting TES and an inductor, as shown in Figure 3a. The inductor is present so that a superconducting quantum interference device (SQUID) can measure the current. These two parallel branches are typically current-biased for stability reasons. Since the shunt resistor has a very low resistance compared to the the superconducting TES branch, the TES is essentially voltage-biased. If the two branches were voltage-biased then the TES would be current-biased and there would be a tendency for it to thermally run away. For example, a small increase in temperature would increase the resistance and that would increase the Joule heating (via $P_{joule} = I^2R$), leading to a positive feedback loop. On the other hand, a voltage-biased TES is self-stabilizing as the Joule heating would decrease (because of $P_{joule} = \frac{V^2}{R}$).

For analysis, we convert this circuit into its Thevenin-equivalent, shown in Figure 3b. Here we label the TES resistance, R_{TES} , the inductance L and the shunt resistor R_L . The TES can have some stray parasitic resistance and inductance, often coming from the wires. However, for our analysis, this can be absorbed into the values of the shunt resistor and the inductor. In other words $R_L = R_{shunt} + R_{parasitic}$ and $L = L_0 + L_{parasitic}$.

From Kirchhoff's second law, the sum of potential differences around this closed circuit is zero, leading to the following equation:

$$V - IR_L - L \frac{dI}{dt} - IR_{TES} = 0. \quad (2)$$

2.1 Linearization

In order to convert Equation (1) and Equation (2) into something we can work with, we linearize everything. By taking first-order Taylor expansions of everything around T_0 , V_0 , I_0 , instead of having unknown functions for things like the TES resistance, they become simple linear functions of δT and δI et cetera. With this we should be able to obtain two coupled first-order differential equations. It's important to note that this linearization is only an approximation valid for small signals, but without it we would not be able to solve the system, because we do not know the functional form of R_{TES} .

In general, R_{TES} is both a function of temperature and current. Therefore we can write the linearized

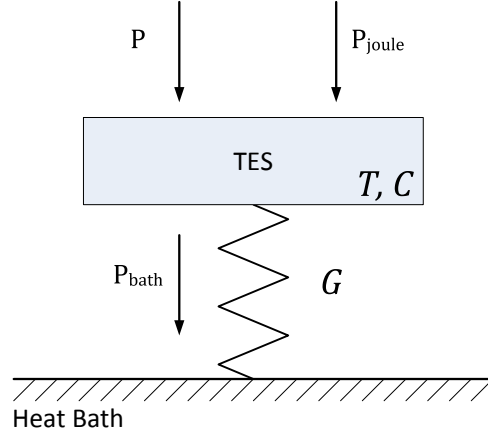


Figure 2: The thermal circuit of an ideal TES.

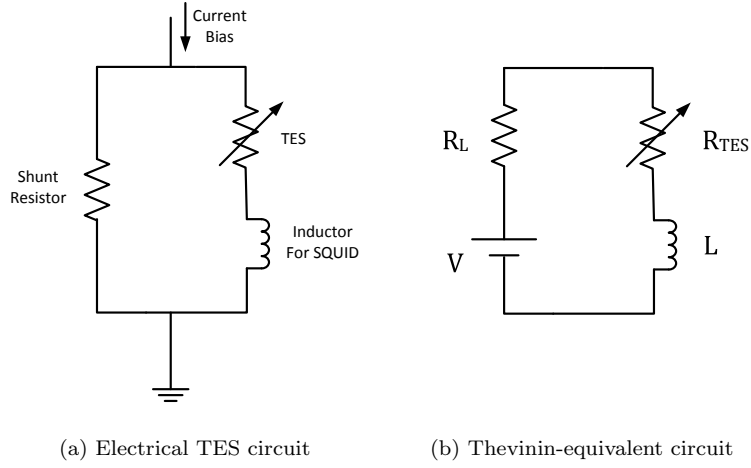


Figure 3: The electrical circuit of an ideal TES. On the left is a typical readout circuit, where the current is measured by a SQUID via the inductor. On the right is its Thevenin-equivalent circuit.

form:

$$R_{TES} = R_0 + \left. \frac{\partial R}{\partial T} \right|_{I_0} \delta T + \left. \frac{\partial R}{\partial I} \right|_{T_0} \delta I \quad (3)$$

$$= R_0 + \frac{R_0}{T_0} \left. \frac{\partial \log R}{\partial \log T} \right|_{I_0} \delta T + \frac{R_0}{I_0} \left. \frac{\partial \log R}{\partial \log I} \right|_{T_0} \delta I \quad (4)$$

$$= R_0 + \frac{R_0}{T_0} \alpha \delta T + \frac{R_0}{I_0} \beta \delta I, \quad (5)$$

where α and β are called the logarithmic temperature sensitivity of the TES resistance and the logarithmic current sensitivity of the TES resistance respectively, and are defined as:

$$\alpha \equiv \left. \frac{\partial \log R}{\partial \log T} \right|_{I_0}, \quad \beta \equiv \left. \frac{\partial \log R}{\partial \log I} \right|_{T_0}. \quad (6)$$

The power to the bath, P_{bath} , can also be expanded to first-order:

$$P_{bath} = P_{bath_0} + \frac{dP_{bath}}{dT} \delta T = P_{bath_0} + G \delta T, \quad (7)$$

where G is known as the thermal conductivity and is defined by:

$$G = \frac{dP_{bath}}{dT}. \quad (8)$$

Finally, the Joule heating also needs to be linearized. The current can be expanded around I_0 as $I^2 = I_0^2 + 2\delta I$, and the resistance can be replaced by the form in (5):

$$P_{joule} = I^2 R = (I_0^2 + 2I_0 \delta I) \left(R_0 + \frac{R_0}{T_0} \alpha \delta T + \frac{R_0}{I_0} \beta \delta I \right). \quad (9)$$

There are now second-order terms caused by $\delta T \delta I$ and $(\delta I)^2$. However, within our first-order approximation for small signals these terms are small compared to the others and can be safely dropped, leaving us with:

$$P_{joule} = P_{J_0} + I_0 R_0 (2 + \beta) \delta I + \frac{P_{J_0}}{T_0} \alpha \delta T. \quad (10)$$

2.2 The coupled differential equations

2.2.1 Electrical

We can substitute our expression for R_{TES} (Equation (5)) into the electrical equation (Equation (2)):

$$V - IR_{th} - L \frac{dI}{dt} - I \left(R_0 + \frac{R_0}{T_0} \alpha \delta T + \frac{R_0}{I_0} \beta \delta I \right) = 0. \quad (11)$$

Given that we have expanded around the I_0 and V_0 when linearizing, we need to rewrite the remaining variables in terms of these. Therefore, $I = I_0 + \delta I$ and $V = V_0 + \delta V$. If we let I_0 and V_0 be the steady state solution to this equation, then they must all cancel by definition. In other words, we are defining them to satisfy $V_0 - (R_{th} + R_0)I_0 = 0$. Any second-order terms that come about, such as $\delta T \delta I$ and δI^2 , are small in this small signal limit and can be ignored. This leaves us with:

$$\frac{d\delta I}{dt} + \frac{(R_{th} + R_0(1 + \beta))}{L} \delta I + \frac{\mathcal{L}G}{I_0 L} \delta T - \frac{\delta V}{L} = 0, \quad (12)$$

where we have defined a new variable, \mathcal{L} , to help simplify things. This is called the low-frequency loop gain under constant current, and is defined as:

$$\mathcal{L} \equiv \frac{P_{J_0} \alpha}{GT_0}. \quad (13)$$

2.2.2 Thermal

We can substitute our expression for P_{bath} (Equation (7)) and P_{joule} (Equation (10)) into the thermal equation (Equation (1)):

$$C \frac{dT}{dt} = P_{J_0} + I_0 R_0 (2 + \beta) \delta I + \frac{P_{J_0}}{T_0} \alpha \delta T + P - P_{bath_0} - G \delta T. \quad (14)$$

Again we expand the power as $P = P_0 + \delta P$ and the temperature as $T = T_0 + \delta T$. The steady state variables must satisfy $P_{J_0} - P_{bath_0} + P_0 = 0$ and therefore cancel, leaving us with:

$$\frac{d\delta T}{dt} - \frac{I_0 R_0}{C} (2 + \beta) \delta I + \frac{G}{C} (1 - \mathcal{L}) \delta T - \frac{\delta P}{C} = 0. \quad (15)$$

2.2.3 Matrix

We can represent the two coupled equations, Equation (12) and Equation (15), in matrix form:

$$\frac{d}{dt} \begin{pmatrix} \delta I \\ \delta T \end{pmatrix} + \begin{pmatrix} \frac{(R_{th} + R_0(1 + \beta))}{L} & \frac{\mathcal{L}G}{I_0 L} \\ -\frac{I_0 R_0}{C} (2 + \beta) & \frac{G}{C} (1 - \mathcal{L}) \end{pmatrix} \begin{pmatrix} \delta I \\ \delta T \end{pmatrix} - \begin{pmatrix} \frac{\delta V}{L} \\ \frac{\delta P}{C} \end{pmatrix} = 0. \quad (16)$$

These are the differential equations that govern the thermo-electrical circuit of an ideal TES bolometer. From this starting point, all the various behaviours of the TES bolometer can be derived. Some examples of things that might be useful to derive are the electrical and thermal responses of the TES bolometer to incoming power signals from photons and the noise spectrum of the TES bolometer.

3 Complex Impedance

One way to test this model is by measuring the impedance of the TES with no photon power input at various frequencies. These experimental data can then be compared to what is predicted by the theoretical model, revealing how accurate the model is.

The model has many unknown parameters that can not be measured directly, such as the logarithmic temperature and current sensitivity, α and β respectively. In order to obtain these parameters, we can use a computer optimization algorithm to fit the experimental data to the theoretical model. These parameters can then be used in other scenarios, such as the predicting the noise spectrum or the TES response.

The main reason we focus on the complex impedance of the TES for this work is that the complex impedance depends on many of the parameters of the model. So, with a single experiment, we are able to determine most of the parameters. The few remaining parameters are measured from other experiments and this is mentioned more explicitly later on.

3.1 Derivation

The complex impedance measurements are made with the TES in the dark. In other words, $\delta P = 0$. To solve the differential equations of Equation (16), we use the technique of harmonic expansion. We expand the input voltage δV in a Fourier series:

$$\delta V = \sum_{\omega} V_{\omega} e^{i\omega t}. \quad (17)$$

Since the differential equations are linear, we can solve them for each ω separately. Given that δI and δT are also Fourier series, differentiation of either results in multiplication by a factor $i\omega$. Putting this all together we arrive at:

$$\mathbf{M} \begin{pmatrix} I_{\omega} \\ T_{\omega} \end{pmatrix} = \begin{pmatrix} \frac{(R_{th} + R_0(1 + \beta))}{L} + i\omega & \frac{\mathcal{L}G}{I_0 L} \\ -\frac{I_0 R_0}{C} (2 + \beta) & \frac{G}{C} (1 - \mathcal{L}) + i\omega \end{pmatrix} \begin{pmatrix} I_{\omega} \\ T_{\omega} \end{pmatrix} = \begin{pmatrix} \frac{V_{\omega}}{L} \\ 0 \end{pmatrix}. \quad (18)$$

To solve this, we take the inverse of the matrix \mathbf{M} :

$$\begin{pmatrix} I_\omega \\ T_\omega \end{pmatrix} = \mathbf{M}^{-1} \begin{pmatrix} \frac{V_\omega}{L} \\ 0 \end{pmatrix}. \quad (19)$$

At this frequency the complex impedance of the entire circuit is the voltage divided by the current:

$$Z_\omega = \frac{V_\omega}{I_\omega} = \frac{V_\omega}{(\mathbf{M}^{-1})_{1,1} \frac{V_\omega}{L}} = \frac{L}{(\mathbf{M}^{-1})_{1,1}}. \quad (20)$$

After doing the rather tedious algebra of inverting the matrix \mathbf{M} , we find the complex impedance of the entire circuit is:

$$Z_\omega = R_{th} + R_0(1 + \beta) + i\omega L + \left(\frac{\mathcal{L}R_0}{1 - \mathcal{L}} \right) \frac{2 + \beta}{1 + i\omega\tau}, \quad (21)$$

where we have defined a new constant, τ , which is some kind of time constant defined by:

$$\tau \equiv \frac{\frac{C}{G}}{1 - \mathcal{L}}. \quad (22)$$

From inspection it is clear that the complex impedance of just the TES, not including the inductor or the shunt resistor, is:

$$Z_{TES} = Z_\omega - R_{th} - i\omega L = R_0(1 + \beta) + \left(\frac{\mathcal{L}R_0}{1 - \mathcal{L}} \right) \frac{2 + \beta}{1 + i\omega\tau}. \quad (23)$$

When plotted parametrically in the complex plane, this traces out a semicircle.

4 Data Analysis

4.1 Transfer Function

The data recorded are the complex values of the transfer function, defined as a function of frequency, f , by the complex ratio of the output signal to the amplitude of an input sinusoidal signal at frequency f on the voltage bias [6, p.51]:

$$T(f) \equiv -\frac{V_{out}}{V_{bias}}. \quad (24)$$

Here, V_{out} is proportional to the current through the inductor L and thus through the TES: $V_{out} = CI$.¹ For every run, we take three sets of transfer functions: one with the TES in the superconducting state, one in the normal state and one at a point in the transition. We are going to label this T_{SC} , T_N and T respectively.

Again we consider the Thevenin equivalent circuit of Figure 3b, except that we have changed R_{TES} to Z_{TES} as we now know that it is complex. We can combine the impedance of the shunt resistor and the inductor through an equivalent impedance: $Z_{eq} = R_L + i\omega L$. Using Ohm's Law and the definition of T we have:

$$I^{-1} = \frac{Z_{eq}}{V} + \frac{Z_{TES}}{V} = -\frac{C}{V_{bias}T}. \quad (25)$$

In the superconducting region, $Z_{TES} = 0$, so the current is:

$$\frac{Z_{eq}}{V} = -\frac{C}{V_{bias}T_{SC}}. \quad (26)$$

¹Specifically, V_{out} is the feedback voltage applied in the servo control loop used to read out the detectors [6].

In the normal region, $Z_{TES} = R_N$, so using the expression in Equation (26), we obtain:

$$-\frac{C}{V_{bias}T_N} = -\frac{C}{V_{bias}T_{SC}} + \frac{R_N}{V}, \quad (27)$$

so that

$$\frac{C}{V_{bias}} \left(\frac{1}{T_{SC}} - \frac{1}{T_N} \right) = \frac{R_N}{V}, \quad (28)$$

leading to:

$$\frac{1}{V} = \frac{C}{R_N V_{bias}} \left(\frac{1}{T_{SC}} - \frac{1}{T_N} \right). \quad (29)$$

Dividing Equation (26) by Equation (29) leads us to:

$$Z_{eq} = -\frac{R_N}{T_{SC}} \left(\frac{1}{T_{SC}} - \frac{1}{T_N} \right)^{-1} \quad (30)$$

For the transition region, from Equation (25) we find:

$$Z_{TES} = \frac{-1}{T} \frac{CV}{V_{bias}} - Z_{eq}. \quad (31)$$

Substituting the expression for $\frac{CV}{V_{bias}}$ from Equation (28) and Z_{TES} from Equation (31):

$$Z_{TES} = R_N \left(\frac{1}{T_{SC}} - \frac{1}{T_N} \right)^{-1} \left(\frac{1}{T_{SC}} - \frac{1}{T} \right). \quad (32)$$

The resistance of the TES in the normal state, R_N , is derived from separate measurements of IV (current-voltage) curves of the TES. For the scope of this paper, we will use the R_N values as given.

4.2 Initial look at the data

The data from a single sensor were transformed according to the function derived in Equation (32) and plotted in Figure 4. The first two graphs plot the real and imaginary parts of Z_{TES} versus frequency. The third plot is a parametric plot of Z_{TES} in the complex plane. In this the curve is traced out from left to right as the frequency increases. Every time the experiment was run, data were taken at three different bias voltages, which correspond to placing the TES in its transition region with resistances of 20%, 50% and 80% of R_N respectively. This is what the three different lines are.

From Figure 4, it is immediately apparent that at high frequencies (above ~ 10 kHz), the data are very noisy. The exact cause of this noise is not known; it occurs during some cryogenic cycles and not others. We anticipate cleaner noise data in the future, but this set is the one we will analyze for this paper.

Since this noisy region would severely affect the data fitting, it is undesirable to keep it. On the other hand, there is something very interesting going on at the high frequencies. This is best seen in the complex plane plot on the right-end of the curve where it begins to bend inwards from a semicircle. Clearly a compromise is needed where we can keep some of this interesting behaviour but remove most of the noise. In our analysis, we exclude data above 9 kHz.

4.3 Fitting

Earlier we derived Z_{TES} as predicted by the ideal model in Equation (23), where there are four parameters (R_0 , β , \mathcal{L} and τ). As mentioned in the previous section, R_0 is actually determined by the voltage bias setpoint and therefore is known. Recall from Equation (22) that τ depends on G , C and \mathcal{L} . The total

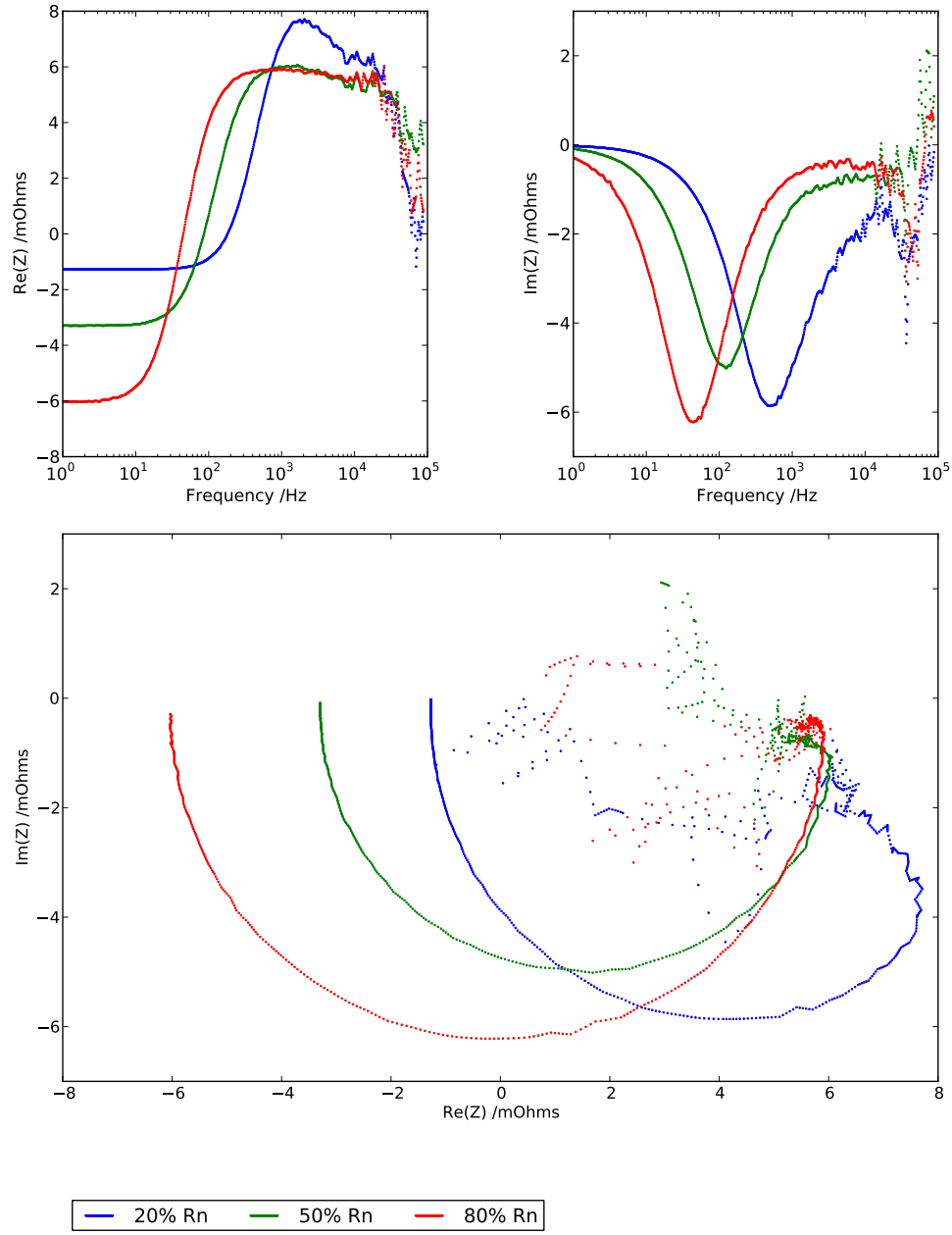


Figure 4: Z_{TES} from a single sensor taken at a temperature of 0.36 K. All three bias setpoints are shown. The top graphs are the real and imaginary parts of Z_{TES} plotted against a logarithmic frequency scale. The lower plot is a parametric plot of Z_{TES} in the complex plane.

thermal conductivity to the bath, G , can be measured from IV curves. Therefore, the fitting program uses an optimization algorithm to fit β , \mathcal{L} and C for the ideal model.

We define an error metric that is summed across all the data point frequencies, where K is some arbitrary constant used for scaling the numbers, very similar to χ^2 . We set $K = 10^6$ to make the error metric near unity for our analysis. The error metric, E , is:

$$E = K \sum |Z_{prediction}(\omega_i) - Z_{measured}(\omega_i)|^2. \quad (33)$$

The optimization algorithms finds the parameters that best minimize the error metric, which, for N parameters, is an $N + 1$ dimensional surface. The algorithm uses a variant of the Powell method. Given some initial guesses for the parameters, it optimizes for the first parameter, by finding the value at which the error is lowest [5, p. 294]. Using this new value for the first parameter, it then proceeds to do the same thing for next parameter. This is iterated cyclically (i.e. after the N th parameter, it starts again at the first parameter) until the parameters no longer change to within some desired precision.

One must be careful, though, that the final parameters are really the global minimum and not a local minimum. Sometimes the results are clearly anomalous and the algorithm can be rerun with new initial guesses. To avoid more subtle failures, we run the program three or four times on each data set with different initial guesses, then choose the results with the lowest error.

Sometimes some of the parameters returned by the fitting algorithm would be negative. However, none of the parameters should be negative. Although the fitting algorithm has no direct method of placing constraints on the parameters, we modified the error metric function to return a very large error when there are any negative parameters. Since the algorithm attempts to minimize this error, the program avoids any negative parameters.

Since the TES heat capacity does not dominate the heat capacity of the bolometer, we expect the total C to be essentially independent of which voltage bias setpoint is examined. (This expectation has been verified in earlier work [6, p. 101].) Thus, we fit data from all three setpoints at once, allowing only the loop gain (\mathcal{L}) and the logarithmic current derivative (β) to vary depending on setpoint.

4.4 Ideal TES

Figure 5 shows the results of fitting the ideal TES model to the bolometer data and the fitted parameters are listed in Table 1. The given parameters are listed in Table 2. The ideal TES model predicts from Equation (23) that the shape of Z_{TES} in the complex plane is a semi-circle. Looking at Figure 5, this is quite accurate at the lower frequencies (the left of the graph). Towards the higher frequencies on the right, however, Z_{TES} begins to deviate from this, exhibiting some inward curvature.

Since the model doesn't exhibit this behaviour, this affects the fitting algorithms, and it becomes inaccurate at the low frequencies too, whilst it tries to fit the semicircle to the high frequencies. This 'hook' is significantly more noticeable at the lowest setpoint (when $R_0 = 20\%R_N$).

This ideal TES model with only one thermal block (namely the TES) clearly is not a very realistic representation of the TES system, as it cannot replicate that high frequency behaviour. Even though it fits relatively well at the low frequencies, the parameters of C , \mathcal{L} and β may not be accurate at all, since they are produced from this inadequate, inaccurate model, and so when they are used in other calculations they may produce the wrong results.

5 Extensions to the ideal TES model

5.1 Two block models

In the ideal TES model, the TES is connected directly to the heat bath by a thermal link of thermal conductivity G . One possible extension to this setup would be add an additional thermal block, which would allow for more complex thermo-electrical behaviour, attached either to the TES or in between the TES and bath. These two possible configurations are shown in Figure 6 and both will be considered below.

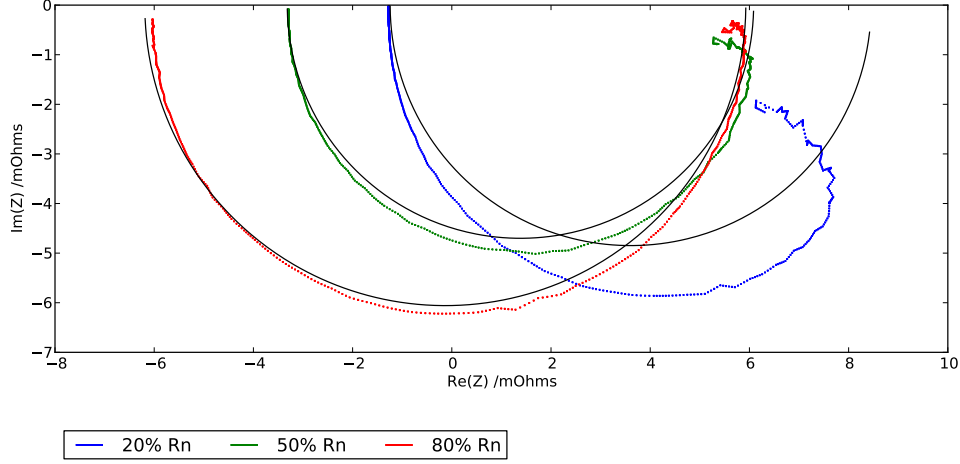


Figure 5: Plots of Z_{TES} (the colored points) for three different points in the transition for a single TES bolometer, at a bath temperature of 0.36 K. The fitted predictions for the ideal TES model are overplotted in black. The fitted parameters are listed in Table 1, whilst the given parameters are listed in Table 2. The ideal model does not capture the high frequency behavior (on the right side of the plot). Data above 9 kHz has not been plotted.

Estimates of the heat capacities in the TES bolometer put the total heat capacity at approximately 0.4 pJ/K, yet the TES itself only accounts for 15% of this total estimate [1]. The remaining 85%, consisting mostly of the silicon nitride substrate that the superconducting TES is mounted on, was not explicitly accounted for in the one block ideal TES model, providing motivation for including a second block. If there were a weak thermal link between the TES and the silicon nitride substrate, this could give the model more accurate behavior.

When multiple thermal blocks are included, we still use the measured total thermal conductivity (from IV curves) from the TES to the bath, G_{total} , as a constraint. For example, in the intermediate-block model (Figure 6a), $G_{total} = G + G_1$, and in the hanging-block model (Figure 6b), $G_{total} = G$.

5.1.1 The derivation of the intermediate-block model

First we consider placing the second block between the TES and bath, as in Figure 6a. If we leave the thermal conductivity of the link from the TES as G , then we can call the thermal conductivity of the link between this intermediate block and the bath G_1 . The heat capacity of the 2nd block is C_1 and the temperature T_1 .

The addition of an extra block has no effect on the electrical circuit; therefore the electrical differential equation in Equation (12) remains the same. The TES thermal differential equation now has an additional term corresponding to the intermediate block: $-\frac{G}{C}\delta T_1$. This adjusts the differential equation to make the heat flow from the TES proportional to the relative temperature difference, $\delta T - \delta T_1$. The thermal differential equation for the new block is (where the second term corresponds to the link to the TES, and the third term is the link to the bath):

$$\frac{d\delta T_1}{dt} + \frac{G}{C_1}(\delta T_1 - \delta T) + \frac{G}{C_1}\delta T = 0. \quad (34)$$

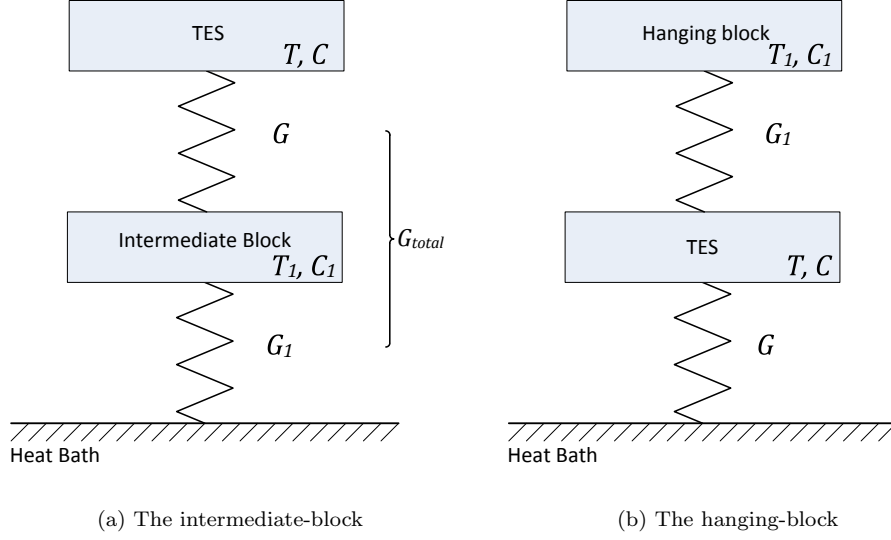


Figure 6: The two possible configurations of the two thermal blocks in a TES bolometer. The additional block could be the silicon nitride substrate that the superconducting TES is mounted on.

Once worked through, we obtain the matrix:

$$\mathbf{M} \begin{pmatrix} \delta I \\ \delta T \\ \delta T_1 \end{pmatrix} = \begin{pmatrix} \frac{(R_{th} + R_0(1+\beta))}{L} + i\omega & \frac{\mathcal{L}G}{I_0 L} & 0 \\ -\frac{I_0 R_0}{C}(2+\beta) & \frac{G(1-\mathcal{L})}{C} + i\omega & -\frac{G}{C} \\ 0 & -\frac{G}{C_1} & \frac{G}{C_1} + \frac{G_1}{C_1} + i\omega \end{pmatrix} \begin{pmatrix} \delta I \\ \delta T \\ \delta T_1 \end{pmatrix} = \begin{pmatrix} \frac{\delta V}{L} \\ 0 \\ 0 \end{pmatrix}. \quad (35)$$

5.1.2 Fitting with multiple blocks

Since \mathbf{M} in Equation 35 is a 3×3 matrix, algebraically obtaining the inverse is tedious. Instead, the fitting program chooses its guess for the parameters and substitutes them in, to get a numerical matrix. Calculating the inverse of this numerical matrix is then trivial. Once the inverse is found, Z_{TES} follows immediately from:

$$Z_{TES} = \frac{L}{(\mathbf{M}^{-1})_{1,1}} - R_L - i\omega L. \quad (36)$$

This approach is identically equivalent to algebraically computing the inverse and substituting in the numerical values afterwards. Whilst large matrices can be algebraically inverted using software such as Mathematica, this method would be more prone to transcription errors, as equations would need to be entered twice: once into Mathematica and once into the source code of the fitting program. The other advantage of numerical inversion is that whenever we change our model and the matrix \mathbf{M} changes, we no longer have to derive a new inverse to get Z_{TES} . Instead, all we need to do is change the elements in \mathbf{M} and the program does the rest for us. This is much faster and easier when trying different models.

However, there is a downside to this, which is in performance. Because ω is one of the parameters of \mathbf{M} , each frequency has a different matrix, and therefore a matrix inversion for each data point has to be done, which can be slow. If one wanted to analyze much larger data sets where performance becomes a concern, it would be best to do the inversion algebraically.

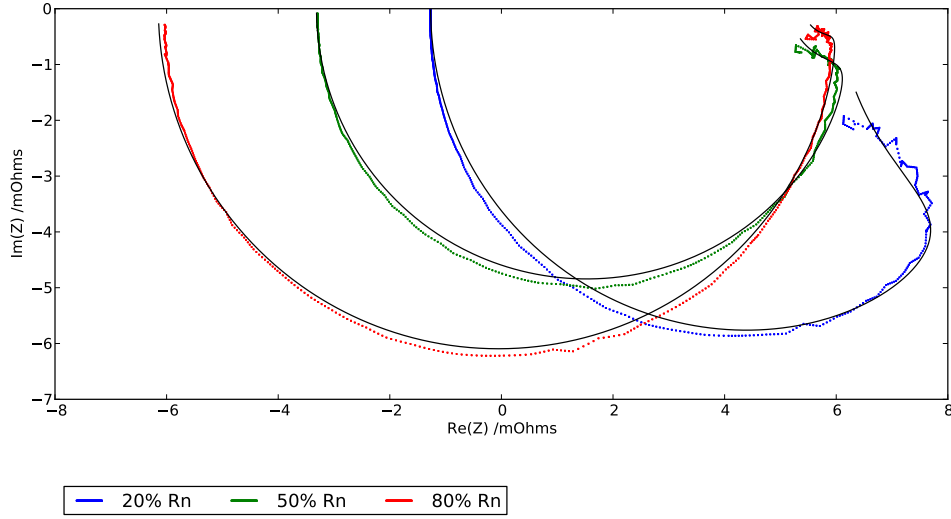


Figure 7: Plots of Z_{TES} (the colored points) for three different points in the transition for a single TES bolometer, at a bath temperature of 0.36 K. The fitted predictions for the intermediate-block model are overplotted in black. The fitted parameters are listed in Table 1, whilst the given parameters are listed in Table 2. The intermediate-block model captures the hook in the data at high frequencies (the right side of the plot). The plotted data are the same as those in Figure 5.

5.1.3 The results of the intermediate-block model fitting

Figure 7 shows the results of fitting this intermediate-block model to the bolometer data previously shown in Figure 5. The fitted parameters are listed in Table 1, whilst the given parameters are listed in Table 2. It is immediately apparent that this is much better than the ideal one block TES model, as at high frequencies the fitted curves bend inwards. This improvement is confirmed by the fact the error metric decreases by a factor of 30 compared to the ideal one block model.

Visually, this seems to be a very close fit throughout the entire frequency range; the largest deviations occur at the very high frequencies at the lowest bias (where R_0 is 20% of R_N). This region is where the systematic noise is worst, so it is not clear if this deviation signifies a shortcoming in the model or in the data.

5.1.4 The hanging-block model

Next we consider placing the second block hanging off the TES, as shown in Figure 6b. We can call the thermal conductivity of the link between the hanging block and the TES block G_1 . The heat capacity of the 2nd block is C_1 and the temperature T_1 .

The TES thermal differential equation now has an additional term corresponding to this additional block that goes on the left hand side of (15): $\frac{G_1}{C}(\delta T - \delta T_1)$. There is also another thermal differential equation for the new block:

$$\frac{d\delta T_1}{dt} + \frac{G_1}{C_1}(\delta T_1 - \delta T) = 0. \quad (37)$$

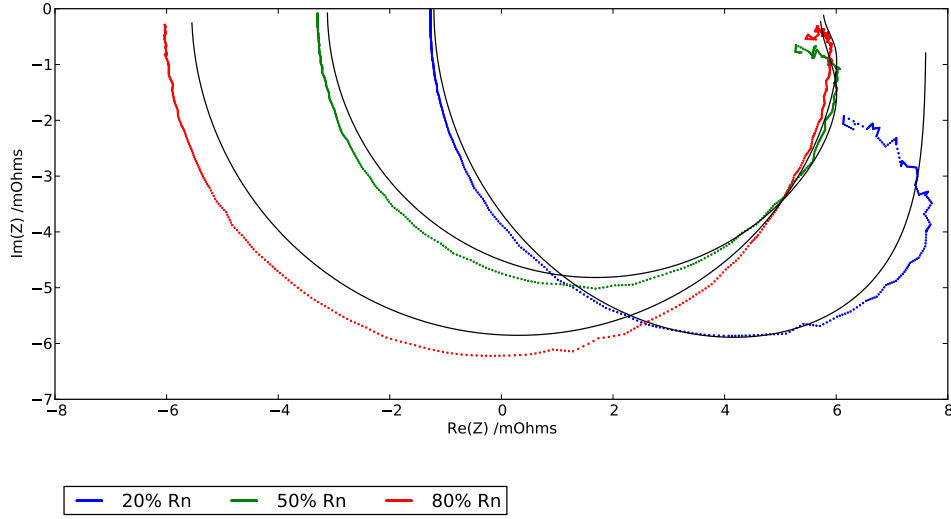


Figure 8: Plots of Z_{TES} (the colored points) for three different points in the transition for a single TES bolometer, at a bath temperature of 0.36 K. The fitted predictions for the hanging-block model are over-plotted in black. The fitted parameters are listed in Table 1, whilst the given parameters are listed in Table 2. Although the hanging-block model is a slight improvement over the ideal model plotted in Figure 5, it does not capture the hook in the data at high frequencies (the right side of the plot) as well as the intermediate-block model plotted in Figure 7. The plotted data are the same as those in Figure 5 and Figure 7.

Once worked through, we obtain the matrix:

$$\mathbf{M} \begin{pmatrix} \delta I \\ \delta T \\ \delta T_1 \end{pmatrix} = \begin{pmatrix} \frac{(R_{th} + R_0(1 + \beta))}{L} + i\omega & \frac{\mathcal{L}G}{I_0 L} & 0 \\ -\frac{I_0 R_0}{C}(2 + \beta) & \frac{G(1 - \mathcal{L})}{C} + i\omega + \frac{G_1}{C} & -\frac{G_1}{C} \\ 0 & -\frac{G_1}{C_1} & \frac{G_1}{C_1} + i\omega \end{pmatrix} \begin{pmatrix} \delta I \\ \delta T \\ \delta T_1 \end{pmatrix} = \begin{pmatrix} \frac{\delta V}{L} \\ 0 \\ 0 \end{pmatrix}. \quad (38)$$

Figure 8 shows the results of fitting this model to the bolometer data previously shown in Figure 5 and Figure 7. The fitted parameters are listed in Table 1, whilst the given parameters are listed in Table 2. This model does not fit the data as well as the intermediate-block model (Figure 7). The improvement over the ideal one-block model (Figure 5) is minor; the error metric decreases by a factor of 2.6. The largest improvement over the ideal model is seen in the lowest setpoint. However, the fits at the other two setpoints are, in fact, slightly worse. This model also does not reproduce the high-frequency bend in Z_{TES} sufficiently. To be sure that this was the global minimum and not a local one, we ran the analysis with many different initial parameter guesses but the results in Figure 8 were the best that we could achieve.

5.2 Verification

To verify our analysis methods, we re-analyzed data from an earlier TES device which has been analyzed in Appel et al. (2010) [1]. We verified the data from the normal and superconducting transfer functions were applied correctly by comparing our Z_{TES} plots to those in Appel et al. (2010). We then verified that our fitting program reproduced the parameters from the intermediate-block model reported in Appel et al.

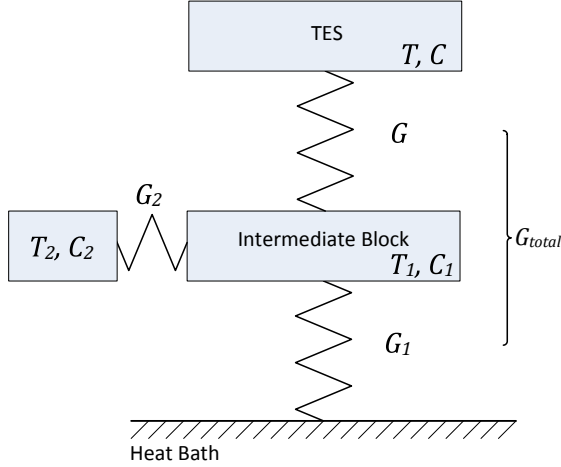


Figure 9: The thermal configuration of the three block model investigated in this paper. This three block model is based off the two block intermediate model as that showed the most improvement. The position of the third block was chosen to match the configuration in Appel et al. (2010) so that comparisons can be made. The fitted constraint given by the measured total thermal conductivity from the TES to the bath in this case is: $G_{total} = G + G_1$.

(2010) to within 10%, consistent with fitting errors and the precision to which the parameters were recorded in Appel et al. (2010).

With the hanging-block model, Appel et al. (2010) also found a similar situation on the earlier TES bolometer that they analysed, where this model did not improve their fits [1]. We re-analyzed data the data from this earlier TES device and came to the same conclusion, as the fits only improved by an insignificant factor of 1.025. Although in our newer TES bolometer we gain a more significant improvement of 2.6 times by going from the one block ideal TES model to the hanging-block model, it still is nowhere near as good as the intermediate-block model which had an improvement of over 30 times.

5.3 Beyond two blocks

Given how much improvement was gained from going from a one-block model to a two-block model, it is only natural to consider more than two blocks. We now consider a three block model.

In the last section, we showed that the intermediate-block configuration seemed to perform better than the hanging-block configuration. Thus, we base our our three block model on the two block intermediate configuration (Figure 6a). There are two possible locations where the third block could be placed: either in series between the TES and the bath, or hanging off the intermediate block. Yue Zhao (2010) examined the configuration where all the blocks are in series, but found that it produced identical fits to the hanging configuration, so we will not consider it [6, p. 117]. Appel et al. (2010) used the hanging configuration [1], so in order to enable comparisons to be drawn between this paper and Appel et al. (2010) we will examine the hanging configuration, as shown in Figure 9.

Figure 10 shows the results of fitting this three block model to the bolometer data previously shown in Figure 5, Figure 7 and Figure 8. The fitted parameters are listed in Table 1, whilst the given parameters are listed in Table 2. Visually this fit looks identical to the two block intermediate configuration as shown in Figure 7. This is reflected by the error metric being virtually the same for both of them.

Examining the parameters in Table 1 closely for this three block model, the thermal conductivity from the intermediate block to the hanging block, G_1 , is many orders of magnitude larger than the other thermal

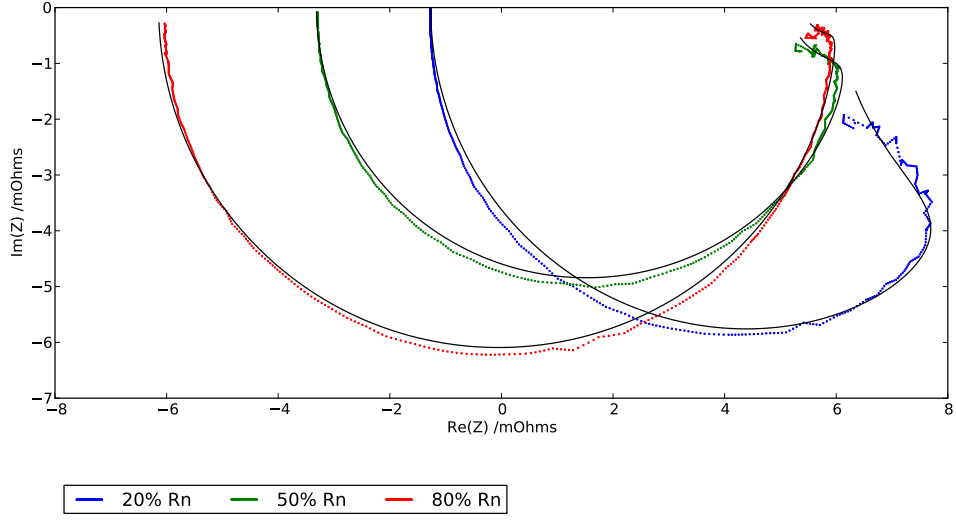


Figure 10: Plots of Z_{TES} (the colored points) for three different points in the transition for a single TES bolometer, at a bath temperature of 0.36 K. The fitted predictions for the three block model are overplotted in black. The fitted parameters are listed in Table 1, whilst the given parameters are listed in Table 2. Whilst the three block model is as good as the intermediate-block model in capturing the behaviour of the TES bolometer, it is no better. The plotted data are the same as those in Figure 5, Figure 7 and Figure 8.

	One block	Two block – intermediate	Two block – hanging	Three block
Error	749	26.3	282	26.3
C/pJK^{-1}	1.50	0.248	1.09	0.248
G/pWK^{-1}	73.8	5,770	73.8	5,790
C_1/pJK^{-1}	–	1.31	1.09	1.06
G_1/pWK^{-1}	–	74.8	5160	74.8
C_2/pJK^{-1}	–	–	–	0.254
G_2/pWK^{-1}	–	–	–	26,400,000
$\alpha^{20\%R_N}$	189	122	221	122
$\alpha^{50\%R_N}$	47.2	42.9	66.8	42.9
$\alpha^{80\%R_N}$	19.6	19.2	28.2	19.2
$\beta^{20\%R_N}$	6.74	4.56	5.97	4.56
$\beta^{50\%R_N}$	1.23	0.898	1.09	0.897
$\beta^{80\%R_N}$	0.357	0.243	0.320	0.244

Table 1: All the parameters that were determined from the fitting for each model at a temperature of 0.36 K. Any given parameters are listed in Table 2. The loop gains, \mathcal{L} s, were converted into logarithmic temperature sensitivities, α s, via the relationship in Equation (13), as this facilitates easy comparison with other papers, where often \mathcal{L} is defined differently (for example in this paper it is defined with G not G_{total}). Errors are dominated by systematic effects due to inadequacies in the fitted models (see Section 6 for further discussion).

conductivities. In this limit, we can treat the intermediate-block and the hanging-block as a single larger thermal block, where the heat capacity is the sum: $C_1 + C_2 = 1.31$ pJ/K. Now note that all the parameters are the same as the two-block model to within small fitting errors.

In other words, to obtain the optimum fit, the fitting algorithm has reduced this three block configuration into an effective two block configuration. This is strong evidence that the three block model isn’t needed since the fitting is preferring the simpler model with less degrees of freedom over this more complex one.

This is in direct contrast to Appel et al. (2010), which found considerable improvement in the fit when the third block was introduced [1]. We re-analyzed the data used in Appel et al. (2010) for the three block case and, indeed, found that the error metric is reduced by a factor of 6 in going from the intermediate-block model to the three block model for those data, which came from an earlier version of the TES bolometer design. We note that those data do not suffer from the high-frequency noise plaguing the current data, but we still observed substantial improvement in going from two to three blocks even after truncating the data at 9 kHz. Perhaps this is evidence that the TES bolometer used for this data has some underlying physical changes compared to the earlier design that Appel et al. (2010) analyzed.

For our data, it seems like the two intermediate block is the best model to use, especially as the additional thermal block can be physically explained by the silicon substrate. The other models, such as the one block or the hanging block model, have much higher error metrics.

6 The Full Data Set

Data were collected on fifteen different TES bolometers, all fabricated from a single design for the ABS experiment [3], at two different bath temperatures.² Here we present results from analysis of all these data, and give estimates of the stability of fitted parameters across the different devices and with different bath temperatures. Note that the errors on the parameters are dominated by systematic effects (see for example Zhao (2010) [6, p. 71]), so examining the stability probes not only the uniformity of the fabrication, but also these systematic errors.

²The data were collected by John Appel and Emily Grace.

Parameter	Value
$G_{total}/\text{pWK}^{-1}$	73.8
P_{J_0}/pW	9.01
$R_N/\text{m}\Omega$	5.46
$R_0^{20\%R_N}/\text{m}\Omega$	1.09
$R_0^{50\%R_N}/\text{m}\Omega$	2.73
$R_0^{80\%R_N}/\text{m}\Omega$	4.37

Table 2: The given parameters for the models analyzed in the single TES analysis sections. The first three parameters are determined from IV curves. The three R_0 s corresponding to each setpoint are chosen, as the TES is biased to meet those points in the transition.

Parameter	Value	Fractional Error	68% Range
$R_N/\text{m}\Omega$	5.26 ± 0.03	0.6%	5.13–5.37
$G_{total}/\text{pWK}^{-1}$	76.8 ± 2.6	3.3%	63.1–85.9
Average Error	37.8		
C/pJK^{-1}	0.255 ± 0.007	2.6%	0.236–0.274
G/pWK^{-1}	6370 ± 200	3.2%	5600–7100
C_1/pJK^{-1}	1.31 ± 0.03	2.4%	1.15–1.42
G_1/pWK^{-1}	77.8 ± 2.6	3.3%	63.9–87.0
$\alpha^{20\%R_N}$	117 ± 12	10.0%	91.6–139
$\alpha^{50\%R_N}$	45.8 ± 1.2	2.7%	41.4–49.9
$\alpha^{80\%R_N}$	20.8 ± 0.4	1.9%	19.3–22.1
$\beta^{20\%R_N}$	4.33 ± 0.41	9.4%	3.53–5.39
$\beta^{50\%R_N}$	0.961 ± 0.046	4.8%	0.773–1.15
$\beta^{80\%R_N}$	0.218 ± 0.011	4.9%	0.165–0.260

Table 3: The mean values of the parameters from the intermediate-block model for a bath temperature of 0.36 K for the fifteen TES bolometers analyzed. The first two parameters listed, R_N and G_{total} , are found from IV curves, whilst the remainder are fitted. The average error is the fitting error, similar to χ^2 , in unnormalized units. The errors listed are the standard errors of the means, with the fractional errors being the fractional standard errors of the means. However, since not all the distributions are Gaussian, the 68% confidence interval is also given.

6.1 Going beyond one sensor

From the single sensor analysis, we concluded the two block intermediate-block model was the best. We fitted data from each of the fifteen bolometers separately. The mean values of the fitted parameters, as well as the standard errors, are reported in Table 3.

Figure 11 and Figure 12 give illustrative histograms for a couple of the fitted parameters: the heat capacity of the intermediate block (C_1) and the heat capacity of the TES (C). Since the distribution in Figure 11 does not look Gaussian, we have put the 68% confidence intervals for the parameters in Table 3. The non-Gaussian spread could be due to actual variation in the devices themselves or to inadequacies in the fitted model.

6.2 Higher temperature

We fitted the 0.46 K bath temperature data and present the results in Table 4. The fits are slightly better at this higher temperature, as shown by the mean error metric decreasing by approximately 15%. Table 5

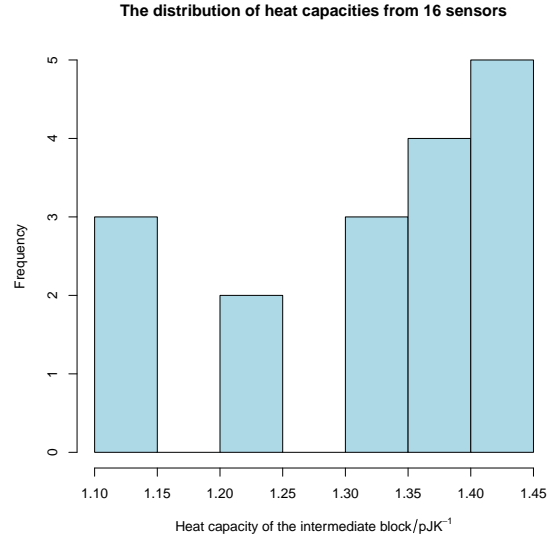


Figure 11: A histogram showing the distribution of heat capacities of the intermediate block (C_1) from the fifteen sensors, taken at a temperature of 0.36 K.

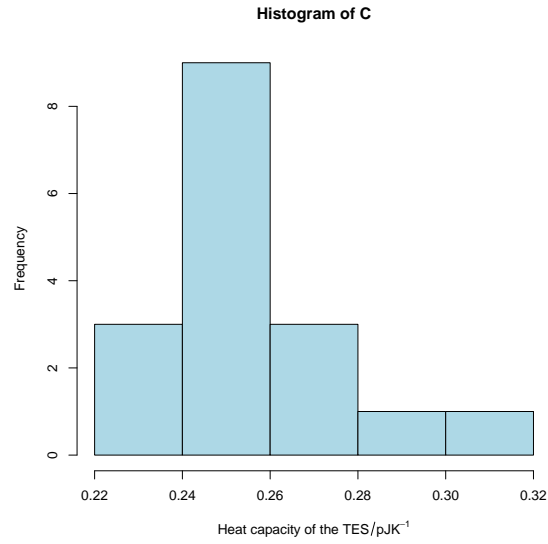


Figure 12: A histogram showing the distribution of heat capacities of the TES (C) from the fifteen sensors, taken at a temperature of 0.36 K.

Parameter	Value	Fractional Error	68% Range
$R_N/\text{m}\Omega$	5.19 ± 0.03	0.7%	5.07–5.32
$G_{total}/\text{pWK}^{-1}$	76.8 ± 2.6	3.3%	63.1–85.9
Average Error	28.2		
C/pJK^{-1}	0.342 ± 0.017	4.9%	0.299–0.357
G/pWK^{-1}	5960 ± 270	4.6%	4970–7010
C_1/pJK^{-1}	1.29 ± 0.04	2.7%	1.12–1.42
G_1/pWK^{-1}	77.8 ± 2.6	3.3%	63.9–87.1
$\alpha^{20\%R_N}$	134 ± 8.7	6.5%	95.0–170
$\alpha^{50\%R_N}$	68.1 ± 3.3	4.9%	60.2–76.2
$\alpha^{80\%R_N}$	32.0 ± 1.1	3.6%	28.6–35.0
$\beta^{20\%R_N}$	3.29 ± 0.23	7.1%	2.24–4.29
$\beta^{50\%R_N}$	0.889 ± 0.057	6.4%	0.763–1.09
$\beta^{80\%R_N}$	0.205 ± 0.016	7.7%	0.158–0.248

Table 4: The mean values of the parameters from the intermediate-block model for a bath temperature of 0.46 K for the fifteen TES bolometers analyzed. The first two parameters listed, R_N and G_{total} , are found from IV curves, whilst the remainder are fitted. The average error is the fitting error, similar to χ^2 , in unnormalized units. The errors listed are the standard errors of the means, with the fractional errors being the fractional standard errors of the means. However, since not all the distributions are Gaussian, the 68% confidence interval is also given.

Parameter	Ratio (0.46 K to 0.36 K)
$R_N/\text{m}\Omega$	0.99 ± 0.01
$G_{total}/\text{pWK}^{-1}$	1.00 ± 0.05
C/pJK^{-1}	1.34 ± 0.07
G/pWK^{-1}	0.94 ± 0.05
C_1/pJK^{-1}	0.98 ± 0.04
G_1/pWK^{-1}	1.00 ± 0.05
$\alpha^{20\%R_N}$	1.15 ± 0.14
$\alpha^{50\%R_N}$	1.49 ± 0.08
$\alpha^{80\%R_N}$	1.54 ± 0.06
$\beta^{20\%R_N}$	0.76 ± 0.09
$\beta^{50\%R_N}$	0.92 ± 0.07
$\beta^{80\%R_N}$	0.94 ± 0.09

Table 5: The ratios of the average parameters at the higher bath temperature of 0.46 K to the average parameters at the lower bath temperature of 0.36 K. The error in this ratio is the standard error coming from the propagation of uncertainty in the mean.

lists the ratios of the average values for the fitted parameters, comparing the 0.46 K bath results to those from the 0.36 K bath.

The parameters characterizing the TES resistance as a function of temperature and current, α and β , change significantly between the two bath temperatures. α increases by between 1 to 9 standard deviations with increasing temperature, and β reduces by between 0.7 to 3 standard deviations with increasing temperature. This is not expected *a priori* since the TES remains at the same transition temperature regardless of the bath temperature.

Although the fits were quite accurate, perhaps the changes in the TES parameters (α and β) with respect to bath temperature indicate a deficiency with the model. If there were some process or parameter that depends on the bath temperature that we had neglected to include in the model, then it might be changing the TES parameters to compensate for the loss of this bath temperature dependent behaviour so that the fits are still accurate. This is like what we had occurring in Section 4.4 with the ideal TES, where the low frequency fit was spoiled by the high frequency fit.

Another possibility is that there is a degeneracy in the model, where several sets of parameters produce the same behavior. For example, there could be no unique α and β for a given data set. However, this seems unlikely as we did not notice any degeneracy in the fitting when we were doing the analysis.

However, with one exception, the thermal properties remain stable. That is, the thermal conductivities, G and G_1 , and the heat capacity of the intermediate block, C_1 , appear approximately independent of bath temperature (to within 1.2 standard deviations). On the other hand, the heat capacity of the TES, C , does increase by almost 5 standard deviations, which is a more significant change.

Since $G \gg G_1$, the intermediate block temperature is similar to the TES (i.e. at its critical transition temperature) and independent of the bath temperature. This implies that G and C_1 are constant as the scenario is the same regardless of bath temperature. Power to the bath is typically assumed to have a power-law dependence: $P_{bath} = K(T_1^n - T_{bath}^n)$ [4]. The thermal conductance, G_1 , is then defined to be: $G_1 \equiv \frac{dP_{bath}}{dT_1} = nKT_1^{n-1}$, which has no dependence on the bath temperature. We have no explanation for why C changes so significantly, but perhaps it is related to the deficiency in the model, as displayed by the TES parameters (α and β) not remaining constant.

7 Conclusion

For the current revision of the TES bolometers that are to be used in the ABS experiment [3], we conclude that the two block intermediate-block model (Figure 6a) seems to be the most suitable. Whilst the Z_{TES} fittings are reasonably accurate, perhaps future experiments could investigate more closely the TES bolometer's behaviour with respect to different bath temperatures. A possible extension to this experiment would be to look at the noise spectra of the TES bolometer, which would provide additional verification of the model. Finally, the total fitted heat capacity for the TES bolometer was approximately 1.6 pJ/K. However, for a similar bolometer Appel et al. (2010) estimated the heat capacity through other methods at approximately 0.4 pJ/K. This disagreement is another thing that could be investigated.

8 References

- [1] J.W. Appel *et al.*, ‘Characterizing and Modeling the Noise and Complex Impedance of Feedhorn-Coupled TES Polarimeters’, (paper presented at the thirteenth international workshop on low temperature detectors, Stanford, USA, 2009).
- [2] J. Bardeen, L.N. Cooper and J.R. Schrieffer, ‘Theory of Superconductivity’, *Phys. Rev.* **108**, 1175 (1957).
- [3] T. Essinger-Hileman *et al.*, ‘The Atacama B-Mode Search: CMB Polarimetry with Transition-Edge-Sensor Bolometers’, arXiv:1008.3915v1 [astro-ph.IM] (2010).

- [4] K.D. Irwin and G.C. Hilton, “Transition-Edge Sensors” in *Cryogenic Particle Detection*, (Springer-Verlag Berlin Heidelberg, 2005).
- [5] W.H. Press *et al.*, “Numerical Recipes: The Art of Scientific Computing”, (1st edition, Cambridge University Press, 1986).
- [6] Yue Zhao, *Characterization of Transition Edge Sensors for the Millimeter Bolometer Array Camera on the Atacama Cosmology Telescope*, (PhD diss., Princeton University, 2010).

9 Source Code

The source code that was used to compute all the plotting and fitting is available in a git repository for viewing and use. The URL is <https://github.com/mileswu/jp1>.

This paper represents my own work in accordance with University regulations. – Miles Wu